RSC Advances

PAPER

View Article Online
View Journal | View Issue

Cite this: *RSC Adv.*, 2025, **15**, 7078

Synthesis of Z-scheme $Ag_4V_2O_7/Ag_3VO_4$/GO nanocomposites for photocatalytic degradation of DDT under visible light†

Giang H. Le, *[ab] Duong A. Thanh,[a] Trang T. T. Pham,[a] Quang Vinh Tran,[ab] Nhiem Ngoc Dao,[bc] Kien Trung Nguyen [c] and Trang T. T. Quan*[a]

The direct Z-scheme $Ag_4V_2O_7/Ag_3VO_4$/GO (AVGZ) nanostructure was successfully synthesized using a hydrothermal method with microwave-assisted techniques. The obtained AVGZ catalyst was characterized by XRD, TEM, EDX, UV-Vis, PL, and XPS methods. The characterization results showed that under controlled pH conditions, the orderly stacking of vanadium oxide tetrahedron formed $Ag_4V_2O_7$ nanoparticles (NPs) on the surface of Ag_3VO_4 nanorods (with a diameter of 50–200 nm). Interestingly, the AVGZ exhibited absorbance in the visible light region at 470–550 nm wavelengths. The photocatalytic performance of AVGZ was evaluated by the degradation of dichloro-diphenyl-trichloroethane (DDT) under LED visible light irradiation. Compared to the $Ag_3VO_4/Ag_4V_2O_7$ nanostructure material, AVGZ showed much higher activity in the degradation of DDT under the same reaction conditions. The optimal conditions were determined to be a catalyst concentration of 0.5 g L^{-1}, pH 6.0, and reaction time of 4 hours, achieving a DDT degradation efficiency of 95.46%, according to the analysis using the response surface methodology (RSM) based on the central composite design (CCD) method. The DDT degradation efficiency was higher compared to Ag_3VO_4/GO (89.4%) and Ag_3VO_4 (82.1%), respectively. Scavenging experiments were conducted to study the photocatalytic mechanism using the spin trapping technique (EPR). The results indicated that ·OH and $\cdot O_2^-$ radicals were the primary oxidizing agents in the photocatalytic reaction process on the AVGZ catalyst. The formation of a heterojunction and the addition of GO accelerated electron–hole pair separation, enhancing the durability and efficiency of the photocatalysts. Furthermore, the Z-scheme mechanism of the AVGZ photocatalyst was also proposed, demonstrating its potential application for DDT degradation under LED visible light.

Received 7th January 2025
Accepted 28th February 2025

DOI: 10.1039/d5ra00134j

rsc.li/rsc-advances

1. Introduction

DDT, dioxin, and furan are listed among the twelve persistent organic pollutants (POPs) under the Stockholm Convention.[1] These substances are thoroughly scrutinized due to their high potential to cause harm to human health and the environment.[2] Various techniques and methods have been developed to remove these pollutants from aquatic environments, such as adsorption, biodegradation, and advanced oxidation processes (AOPs).[3–5] The biological treatment approach is inefficient and takes a long process, while the adsorption method is not comprehensive and can result in secondary contamination.[3] Heterogeneous photocatalysis, classified as an AOP, has garnered significant interest from researchers as one of the green and efficient methods for DDT removal. This method utilizes photo-generated electrons (e^-) with strong reduction potential and holes (h^+) with strong oxidation potential produced during the reaction.[6,7] Consequently, many photocatalysts, such as TiO_2,[8] ZnO,[9] and $BiSbO_4$,[6] have been developed. However, these single-component catalysts often suffer from fast electron–hole (e^-/h^+) recombination rates and poor activity in the visible light region, which greatly limits their applications.[10] To address these limitations, several research groups have designed heterostructured catalysts, such as $SrTiO_3/Ag_2O^7$ and Ag_2O/CuO,[11] to suppress e^-/h^+ recombination and thereby enhance DDT degradation efficiency in water. Based on different electron transfer mechanisms, heterojunctions can be classified into Type I, Type II, p–n junctions, Z-scheme, and S-scheme structures.[12] In photocatalytic reactions, Type I and Type II heterojunctions perform less well because of their inadequate electron separation and transport.[13] In

[a]*Institute of Chemistry, Vietnam Academy of Science and Technology, 18 Hoang Quoc Viet, Cau Giay, Hanoi 100000, Vietnam. E-mail: giangnasa86@gmail.com; quanthutrang5986@gmail.com*

[b]*Graduate University of Science and Technology, Vietnam Academy of Science and Technology, 18 Hoang Quoc Viet, Cau Giay, Hanoi 100000, Vietnam*

[c]*Institute of Material Science, Vietnam Academy of Science and Technology, 18 Hoang Quoc Viet, Hanoi 100000, Vietnam*

† Electronic supplementary information (ESI) available. See DOI: https://doi.org/10.1039/d5ra00134j

comparison to Z-scheme and S-scheme systems, their light absorption and spectral utilization capacities are likewise more constrained, and the energy conversion efficiency is decreased by the quick recombination of electron–hole pairs. Z-scheme heterojunction effective electron separation and transfer processes maximize photocatalytic activity, which raises reaction efficiency.[12,14] Thus, one of the most essential methods for enhancing photocatalytic performance is the construction of heterostructures, especially Z-scheme heterojunctions.[15]

Silver vanadate-based catalysts supported on various materials exhibit photocatalytic activity in the visible light region due to their narrow bandgap energy (E_{bg}) ranging from 1.9 to 2.5 eV, making them promising candidates for the effective degradation of organic dyes and their conversion into water and carbon dioxide.[15] Previous studies indicate that silver vanadate exists in four main phases, including $AgVO_3$, $Ag_2V_4O_{11}$, Ag_3VO_4, and $Ag_4V_2O_7$, with the Ag_3VO_4 phase demonstrating the highest photocatalytic activity.[16]

Graphene oxide (GO) of the graphene family is a preferred support material due to its large surface area, visible light absorption capability, and high electron transport properties, which effectively reduce e^-/h^+ recombination.[2,17] Consequently, many heterostructured photocatalysts based on Ag_3VO_4 and graphene oxide, such as Ag_3VO_4/rGO,[18] Ag_3VO_4/WO_3/rGO,[17] Ag_3VO_4/TiO_2/graphene,[19] and g-C_3N_4/Ag_3VO_4/rGO,[20] have been extensively studied in recent years. However, these systems have primarily been utilized for the degradation of dyes, phenols, and antibiotics.[16,17,21] Research on DDT degradation using Ag_3VO_4-based catalysts remains limited.

In this study, Z-scheme heterostructured photocatalysts $Ag_4V_2O_7/Ag_3VO_4$/GO (AVGZ) and Ag_3VO_4/GO (Ag3V) were designed using Ag_3VO_4, $Ag_4V_2O_7$, and GO synthesized through a hydrothermal-microwave-assisted method to overcome the limitations of individual materials. Modern characterization techniques, including XRD, TEM, BET, XPS, PL, and UV-Vis, were employed to demonstrate that GO effectively disperses Ag_3VO_4 and $Ag_4V_2O_7$ NPs, enhances surface area, and reduces e^-/h^+ recombination in the composite catalysts. The photocatalytic activity of these nanocomposite catalysts was tested for DDT degradation in aqueous solutions under visible LED light irradiation (400–650 nm). To evaluate the interactions among operational factors influencing the reaction process, the RSM-CCD method was applied. Based on the analysis of reactive species involved in the reaction and the E_{bg} of semiconductor materials in the catalysts, a preliminary photocatalytic mechanism for DDT degradation on the catalyst systems was proposed.

2. Experimental

2.1. Chemicals

All chemicals, including 4,4-dichlorodiphenyltrichloroethane (DDT), $AgNO_3$, NH_4VO_3, graphite (C), NH_4OH, acetone, *n*-hexane, dichloromethane, 5-dimethyl-1-pyrroline-*N*-oxide (DMPO), *tert*-butyl alcohol, *p*-benzoquinone, and ammonium oxalate ($(NH_4)_2C_2O_4$) at analytical grade were purchased from Merck and used directly without any further purification. High-purity N_2 (99.99%) and O_2 (99.99%) gas cylinders were supplied by Venmer, Vietnam. Single-distilled water was used for all synthesis and processing procedures.

2.2. Synthesis of AVGZ nanostructured catalyst

GO, which was generated using the modified Hummer's process as previously reported,[2] served as the support for the microwave-assisted hydrothermal approach used to create the AVGZ catalyst (Ag/V = 3 : 1). To create solution A, 5.0 wt% of GO was dissolved in 60 mL of distilled water/ethanol (1 : 1 volume ratio) and sonicated for ten minutes. Solution B was created by fully dissolving 1.02 g of $AgNO_3$ in 80 mL of water. Drop by drop, solution B was added to suspension A, and the mixture was agitated for 30 minutes at 250 rpm. Solution C was prepared by dissolving 0.234 g of NH_4VO_3 completely in 100 mL of distilled water at 60 °C. After mixing suspension A and solution B, solution C was gradually added to the mixture and further stirred at 500 rpm for 1 hour. The pH of the mixture was adjusted to 8.0 using NH_4OH 25% and HNO_3 0.1 mol L^{-1} solutions. The product gradually changed color from dark brown to deep yellow. The resulting mixture was then transferred to a 300 mL Teflon vessel and subjected to microwave irradiation for 30 minutes at 130 °C. The obtained product was filtered, washed with distilled water until pH 7.0, and dried at 100 °C for 6 hours to remove residual water.

For comparison, Ag3V and Ag_3VO_4 were also synthesized using the described method with pH 13 and (Ag/V = 3 : 1). A single-phase $Ag_4V_2O_7$ (Ag4V) with a Ag/V ratio of 2 : 1 at pH 9 was prepared in the absence of GO.

2.3. Material characterization

The nanocomposites AVGZ, Ag3V, Ag4V, Ag_3VO_4, and GO were characterized using various techniques. X-ray diffraction (XRD) patterns were obtained using a D8 Advance (Germany). Transmission electron microscopy (TEM) images were recorded with a HITACHI-H-7500 (Japan). Brunauer–Emmett–Teller (BET) surface area measurements were performed with a Trista Plus II, Micromeritics (USA). The valence states and chemical bonding of the catalysts were analyzed by X-ray Photoelectron Spectroscopy (XPS) on a THERMO VG SCIENTIFIC (UK), MultiLab 2000. The optical properties of the catalysts were evaluated through UV-Vis DRS spectra. Electrochemical measurements were carried out using a Zahner Zennium Pro (Zahner-Elektrik, Germany) at room temperature. The EPR technique (ER200-SRC-10/12, Bruker E580) with 5,5-dimethyl-1-pyrroline-*N*-oxide (DMPO) as a spin trap for ·OH and O_2^- radicals was employed to detect reactive oxygen species (ROS) under LED light irradiation.[22] Scavengers including *p*-benzoquinone (2.0 mg), N_2 (20 mL min^{-1}), *tert*-butyl alcohol (TBA, 2 mL), and ammonium oxalate (AO, 0.2 g) were used to quench O_2^-, ·OH, and h^+ species in the reaction.

2.4. Photocatalytic activity on materials

The photocatalytic degradation of DDT was conducted in an aqueous solution at room temperature using a Julabo U3 cooling system. A 50 W LED with a wavelength range of 400–650 nm

was used as the source of visible light. The LED light source we employed for our research had an irradiance of roughly 1200 lux. The distance between the light source and the surface of the dye solution was maintained at 20 cm. During the photocatalytic degradation of DDT at a concentration of 10 mg L^{-1}, 200 mL of reaction medium (water/acetone in a 9 : 1 volume ratio) was used. The catalyst dosage (cat.) was maintained within 0.1–0.5 g L^{-1}, while the pH was varied from 3.0 to 9.0 and the stirring speed was set at 250 rpm to determine the optimal conditions for the process. Prior to photocatalysis, the system was kept in the dark for 30 minutes to achieve adsorption equilibrium. At specific time intervals, 3 mL samples were withdrawn and treated with two drops of 0.1 N $Na_2S_2O_3$ to quench residual ROS. The concentrations of DDT and intermediate products were analyzed using the EPA 8081A method on a GC-MS system (Agilent GC 7890A, MS 5975C) equipped with a DB5 column. Experiments were repeated three times with standard deviations (SD) less than 5.0%. Post-reaction catalysts were collected by centrifugation at 5500 rpm, washed, dried, and replenished to account for mass loss (<5.0%) for repeated experimental cycles. DDT removal efficiency (H%) and reaction rate constant (k_{vis}) are calculated using the following formula: eqn (1.4) and (1.5) (ESI†).

3. Results and discussion

3.1. XRD pattern analysis

Fig. 1a shows the XRD pattern of GO, exhibiting peaks at $2\theta \sim 10.5°$ and 43.9°, attributed to the (002) and (100) reflection planes in graphene oxide materials, indicating a large number of oxygen-containing functional groups.[23] The XRD pattern of Ag_3VO_4 displays peaks at 19.1°, 30.9°, 32.3°, 35.1°, 35.9°, 38.9°, 51.4°, and 54.1°, corresponding to the crystal planes (011), (−121), (121), (301), (022), (−330), and (331), which match the standard X-ray diffraction data JCPDS-430542 with a monoclinic Ag_3VO_4 structure and high crystallinity.[20] The XRD patterns of Ag3V and AVGZ show reduced intensities of characteristic peaks of Ag_3VO_4, and no distinctive GO peaks are observed (Fig. 1b). This is explained by the attenuation of the carbon signal caused by Ag_3VO_4 NPs intercalating between GO layers.[18,24] At low pH (6.0–7.0), the predominant phase is $AgVO_3$ due to the dominance of VO_3^- groups.[25] When the pH increases to 9.0–14.0, VO_3^- becomes unstable, forming $V_2O_7^{4-}$ and VO_4^{3-} phases, which lead to $Ag_4V_2O_7$ and Ag_3VO_4 NPs anchored on GO layers.[26] However, at pH 8.0–10.0, the conversion of VO_3^- to $V_2O_7^{4-}$ occurs, with some converting to VO_4^-, forming nanocomposites of $Ag_4V_2O_7$ and Ag_3VO_4 anchored on GO layers, resulting in the AVGZ material.[27] The XRD patterns in Fig. 1b show that Ag3V and Ag4V exhibit characteristic peaks consistent with XRD data JPCDS-0097 and JPCDS-0542, confirming the presence of $Ag_4V_2O_7$ and Ag_3VO_4 phases. For AVGZ, peaks at 31.02° and 32.45° indicate the presence of Ag_3VO_4, while peaks at 32.01° and 33.05° confirm the presence of $Ag_4V_2O_7$, respectively.[28,29] The slight shifts in peak positions compared to standard cards may result from the influence of GO in the material structure.

3.2. Morphological characterization of the materials

The TEM images of the materials are shown in Fig. 2. The controlled crystal structure during synthesis alters the shape of the samples. Fig. 2a shows $Ag_4V_2O_7$ NPs with a size of 200 nm. The Ag_3VO_4 NPs have a size of approximately 50 nm and aggregate into larger clusters (Fig. 2b). For AVGZ, $Ag_4V_2O_7$ particles of 30–50 nm size are anchored onto the Ag_3VO_4 nanorods, which have a 1D structure (Fig. 2d). During the phase transition, $Ag_4V_2O_7$ precipitates from the $AgVO_3$ nanorods as the pH increases to form a more stable crystalline structure.

Furthermore, the XRD pattern only shows the predominant presence of two phases, $Ag_4V_2O_7$ and Ag_3VO_4, indicating that the 1D structure in the AVGZ material is attributed to the Ag_3VO_4 phase. These results are consistent with previous reports.[26,27] The TEM image in Fig. 2c shows that GO has a 2D nanostructure with surface folds formed by multiple stacked layers. When GO sheets are used as a support material, they prevent aggregation and help the NPs distribute more evenly. This confirms that the layers of GO reduce the particle size and limit the aggregation of NPs in the resulting composite nanomaterial system.[30]

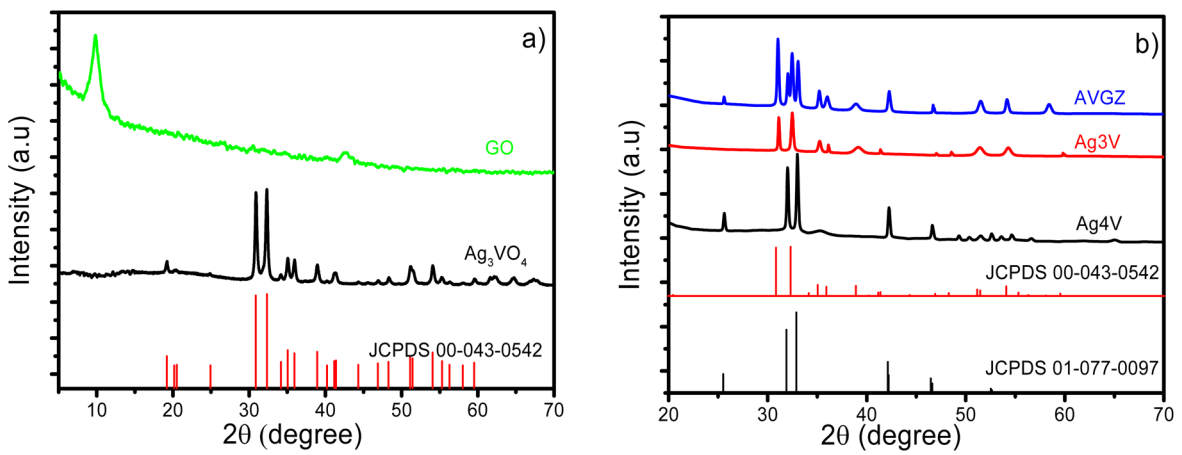

Fig. 1 XRD patterns of GO (a), Ag_3VO_4 (a), Ag3V (a and b), Ag4V (b), and AVGZ (b).

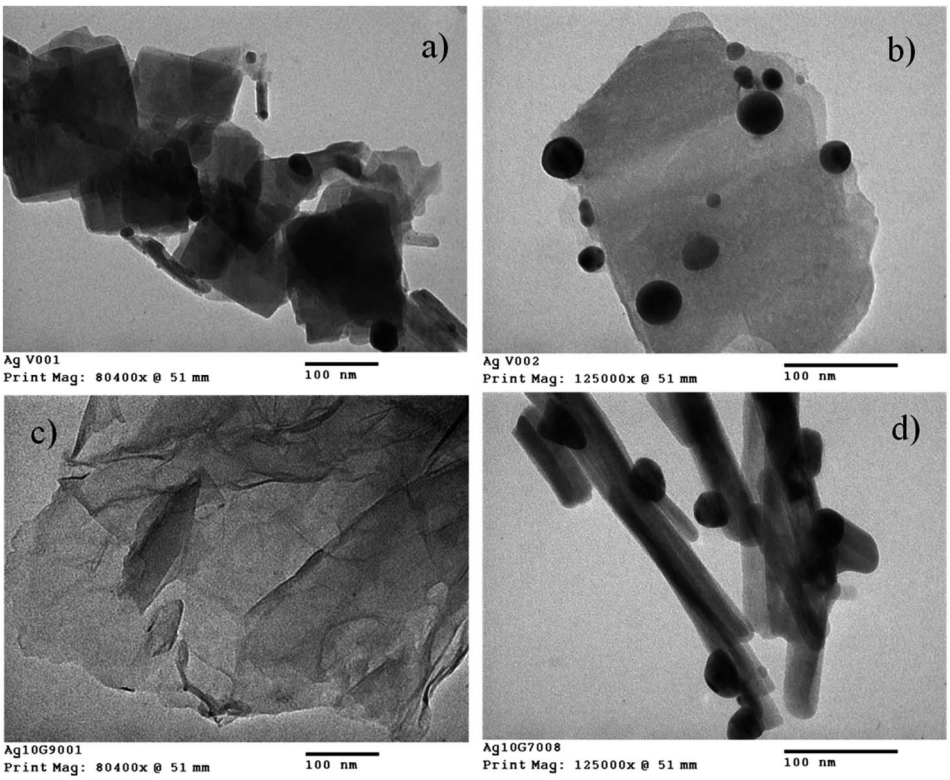

Fig. 2 TEM images of $Ag_4V_2O_7$ (a), Ag3V (b), GO (c), and AVGZ (d).

3.3. Surface properties analysis of the materials

The results of BET measurements for the GO, AVG, and Ag_3VO_4 samples are presented in Fig. 3. The adsorption–desorption isotherms of the materials (Fig. 3a) show that at low relative pressure (P/P_0) values (0–0.3), monolayer adsorption occurs on the catalyst surface. Multilayer adsorption and capillary condensation within the pores begin at higher relative pressures (0.3–0.4). All the samples have large pore sizes (12–20 nm), resulting in strong capillary condensation, with a wide H1 hysteresis loop of type IV, according to the IUPAC classification, between the adsorption and desorption branches.[31] The pore distribution results in Fig. 3b indicate that the AVGZ composite material is porous. The addition of GO to the Ag_3VO_4 and $Ag_4V_2O_7$ materials contributes to an increase in surface area, primarily due to the large specific surface area and strong adsorption capacity of GO. Table 1 shows the surface areas of GO, Ag_3VO_4, Ag3V, Ag4V, and AVGZ as 336.0, 4.4, 36.2, 6.2, and 11.4 $m^2\ g^{-1}$, respectively. The specific surface area of Ag3V is higher than that of Ag4V and AVGZ because, in Ag3V, the Ag_3VO_4 NPs exist in smaller sizes, while in AVGZ, Ag_3VO_4 has a 1D nanorod shape. The micropore volume of the materials increases with the presence of GO, which enhances the

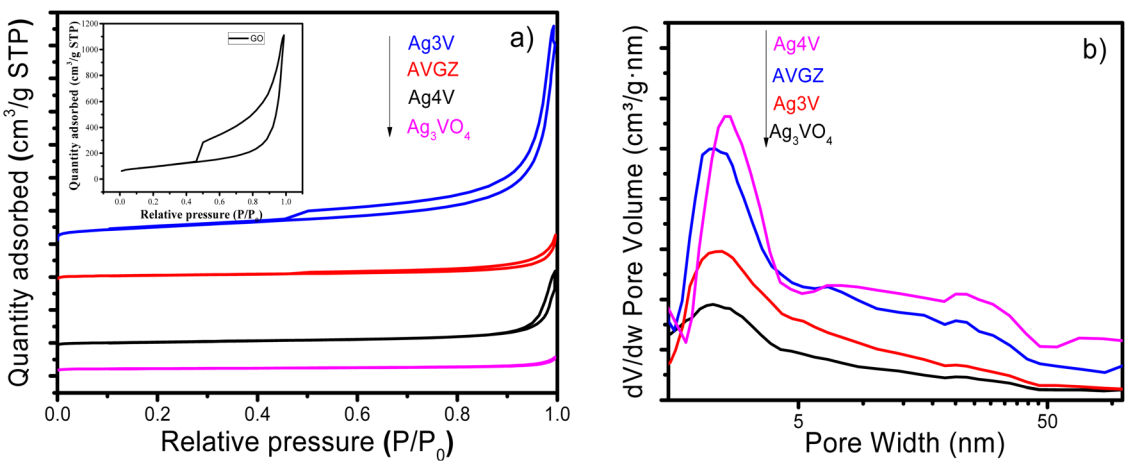

Fig. 3 Nitrogen adsorption–desorption isotherms at 77 K (a) and pore size distribution (b) of the materials.

Table 1 Characteristic parameters of Ag_3VO_4, Ag3V, Ag4V, AVGZ, and GO according to the BET method

Measurement	GO	Ag_3VO_4	Ag3V	Ag4V	AVGZ
S_{BET} ($m^2\ g^{-1}$)	336.0	4.4	36.2	6.2	11.4
$V_{micropore}$ ($cm^3\ g^{-1}$)	0.0020	0.0011	0.0050	0.0009	0.0024
V_{pore} ($cm^3\ g^{-1}$)	1.719	0.013	0.036	0.033	0.051
D_{nm} (nm)	20–21	12.2–13.7	19.2–20.9	12.1–14.4	17.8–23.8

advantage in photocatalytic reactions due to the high affinity of these micropores for pollutants. Additionally, when the surface area increases, it boosts the adsorption capacity for contaminants, which is beneficial for increasing the contact area between free radicals, active sites, and pollutants, thus enhancing catalytic performance.[24,30,32]

3.4. X-ray photoelectron spectroscopy (XPS)

XPS determined the oxidation states and bond energies of the samples. The XPS spectrum (Fig. S1†) for GO shows that it is highly pure since it only contains carbon (C) and oxygen (O). Fig. 4a shows the full spectrum of Ag_3VO_4, Ag3V, and AVGZ, confirming the presence of the elements Ag, V, O, and C in the materials. Fig. 4b shows the Ag 3d spectrum of Ag_3VO_4, with peaks at energy levels of 368.7 and 374.7 eV, corresponding to the Ag $3d_{3/2}$ and Ag $3d_{5/2}$ oscillations of Ag^+ in the monolithic Ag_3VO_4 structure.[24] These peaks are slightly shifted to 369.2 and 375.3 eV for Ag3V and to 368.2 and 374.3 eV for AVGZ, respectively. This trend is also observed in the V 2p spectrum (Fig. 4c). The binding energies of V $2p_{1/2}$ and V $2p_{3/2}$ in Ag_3VO_4 are 524.0 and 516.5 eV, confirming the presence of V^{5+}.[24,30] These binding energies shift to 524.2 and 516.7 eV in Ag3V and 523.9 and 516.7 eV in AVGZ, respectively. This confirms that GO slightly affects the oxidation states of the constituent elements in the composite nanomaterial.[24,32,33] The C 1s spectrum in Fig. 4d shows that GO contains many oxygen-containing functional groups corresponding to C–C (284.6 eV), C–O (286.3 eV), and C═O (288.4 eV) bonds. The C 1s spectra of AGVZ showed

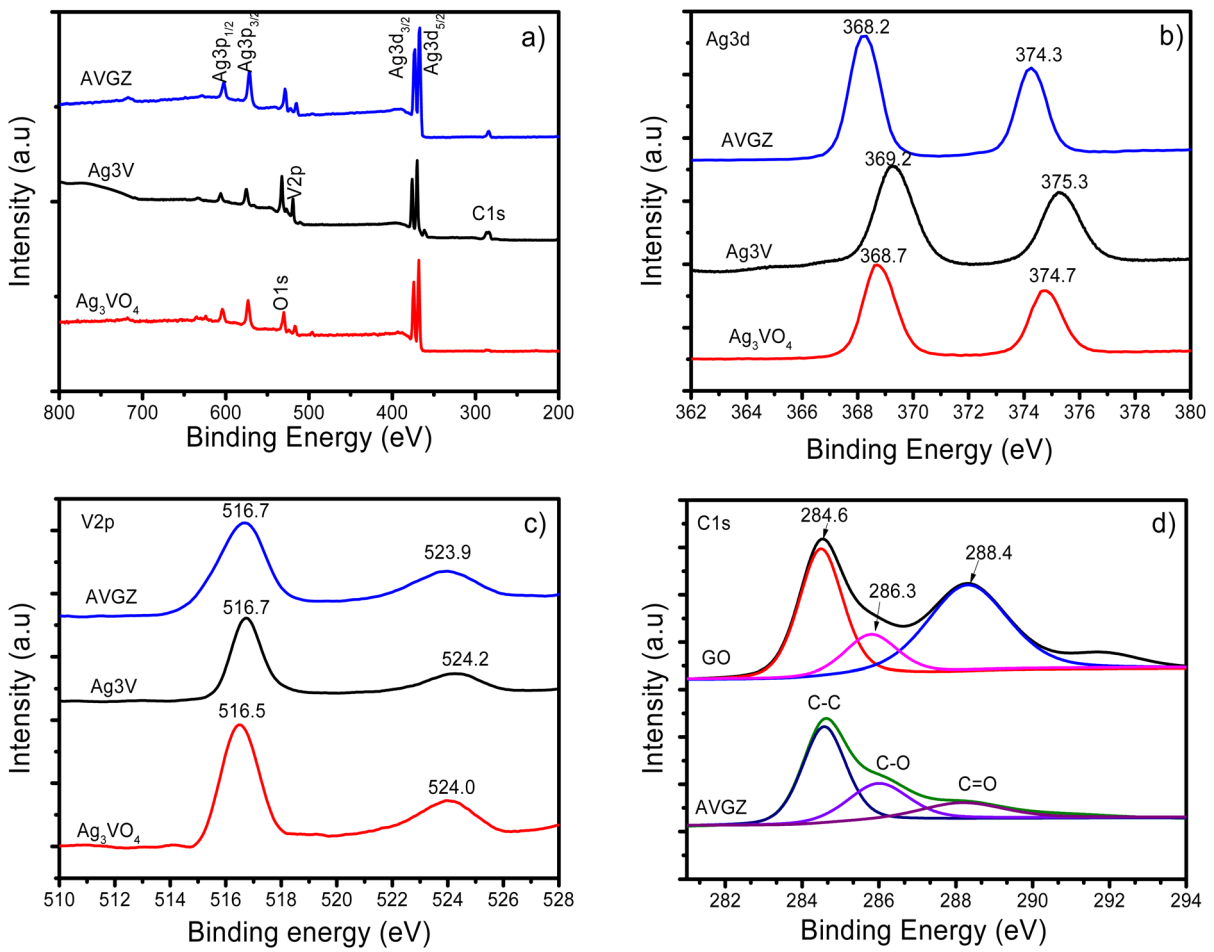

Fig. 4 (a) The XPS scan with the respective high-resolution spectra of (b) Ag 3d, (c) V 2p, and (d) C 1s core level of Ag_3VO_4, Ag3V, AVGZ and GO catalysts.

a positive shift of 0.1 to 0.2 eV. The formation of metal–oxygen–carbon (M–O–C) bonds as a result of electron transfer from NPs to GO is responsible for this shift. Furthermore, GO has high resistivity, which causes it to behave like an insulator by disrupting the sp^2 bonding network, may have an impact on the chemical and electrical states of the GO materials.[32] This demonstrates that GO is present in the composite material and that the strong covalent bonds between the GO layers and nanoparticles create an M–O–C electron transport channel.[18,21] This result is also consistent with the previous XRD and TEM analyses.

3.5. UV-Vis absorption spectra (DRS) and photoluminescence (PL) analysis

The results shown in Fig. 5a indicate that the DRS of Ag_3VO_4 and Ag4V have peaks at 400 nm, with the absorption edge mostly located at 560 nm. In the materials Ag3V and AVGZ, the absorption peaks shift to 450 nm, and the visible light absorption edge is stronger compared to the individual components Ag_3VO_4 and $Ag_4V_2O_7$. This confirms that all the materials have the ability to absorb visible light radiation. The band gap energies of the Ag3V and AVGZ materials were determined using K–M and Bo Weng (Fig. 5b), with values of 2.19 and 2.35 eV, respectively. For Ag_3VO_4 and Ag4V, the band gap energies are 2.32 and 2.48 eV, respectively.[24,32,34]

According to the EIS diagrams, AVGZ has the shortest arch radius of all the catalyst samples (Fig. S2a†). The PL spectrum of the steady-state emission (Fig. S2b†) follows the intensity order of Ag_3VO_4 > Ag3V > AVGZ, suggesting that AVGZ possesses the fastest charge separation and the lowest charge transfer resistance. This is attributed to the enhanced local electric field, which provides favorable conditions for photocatalytic reactions.[35,36] This implies that Ag_3VO_4 alone does not have as strong a photocatalytic activity as AVGZ and Ag3V.

3.6. Photocatalytic activity

The catalytic activity for DDT degradation under LED light and the adsorption equilibrium state in solution on the catalysts are presented in Fig. 6 and S3.† As depicted in Fig. S3,† the adsorption capacity of the catalyst samples remains essentially unchanged after 30 to 60 minutes of adsorption in the dark, indicating that the catalysts have reached adsorption–desorption equilibrium. As seen in Fig. 6a, the DDT adsorption capacity at pH 6 for the GO-containing catalysts is higher than that of pure Ag_3VO_4. This is attributed to the contribution of the surface area and the strong π–π interactions between GO and the aromatic ring of DDT.[2] Furthermore, the results confirm that no degradation was observed when irradiation was applied in the absence of a catalyst. After 4 hours of reaction, the DDT decomposition rate (k_{vis} min^{-1}) decreased in the following order: AVGZ (0.0162) > Ag3V (0.0119) > Ag4V (0.0108) > Ag_3VO_4 (0.0085) (Fig. 6b). This indicates that GO enhances the adsorption capacity and introduces more active sites to interact with the organic pollutant DDT.[37] The DDT degradation activity of the GO-doped catalytic systems is higher than that of Ag_3VO_4, as the presence of GO enhances visible light absorption, extends the lifetime of free electrons, and inhibits the recombination of e^-/h^+.[24] Additionally, catalyst stability is a crucial parameter for large-scale applications. The results in Fig. 6c show that after 4 reaction cycles, the catalytic activity of AVGZ still maintains 80% efficiency. This confirms that coupling with GO improves the overall stability of the catalyst, prolonging its operational cycle.[37] However, the inclusion of GO only marginally mitigates the photochemical corrosion that is present in all species of silver vanadate. The production of β-$AgVO_3$, Ag_2O, or Ag^0 phases may result from the photochemical corrosion of Ag_3VO_4 and $Ag_4V_2O_7$, which causes the catalytic activity of AVGZ to decrease in the fourth cycle.[32]

The effect of pH on catalytic activity was studied and presented in Fig. 6d. As is well known, DDT is a non-polar organic chlorine compound, poorly dissociating in water, and does not exhibit clear ionization states like strong acids or bases. Therefore, the DDT degradation efficiency depends on the interaction between the catalyst surface and the DDT molecule and the production rate and quantity of ROS species in the reaction. Fig. 6d shows that in a strongly acidic environment with abundant h^+, the formation of ·OH radicals may be

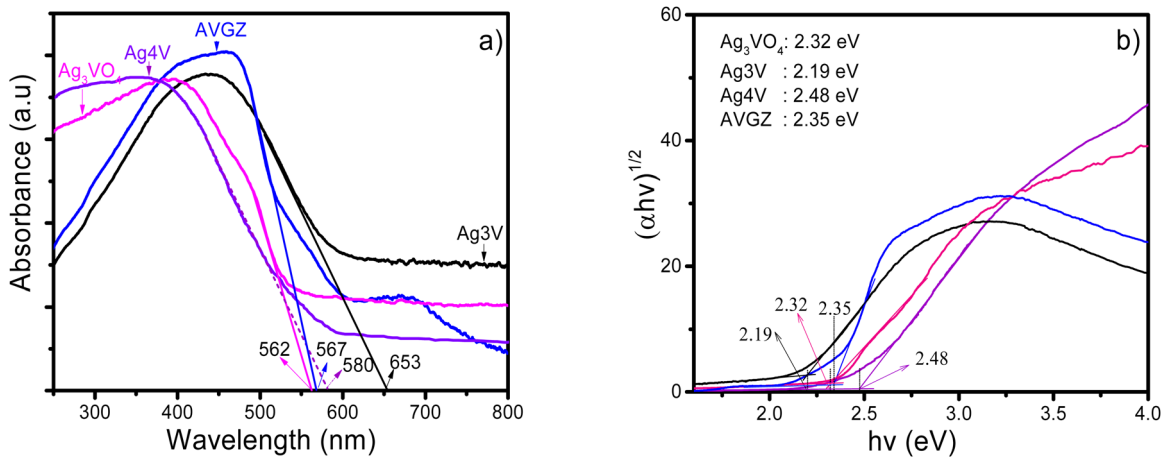

Fig. 5 UV-Vis absorption spectra (a) and E_{bg} calculation (b) using the Kubelka–Munk method (K–M) of Ag_3VO_4, Ag3V, Ag4V, and AVGZ.

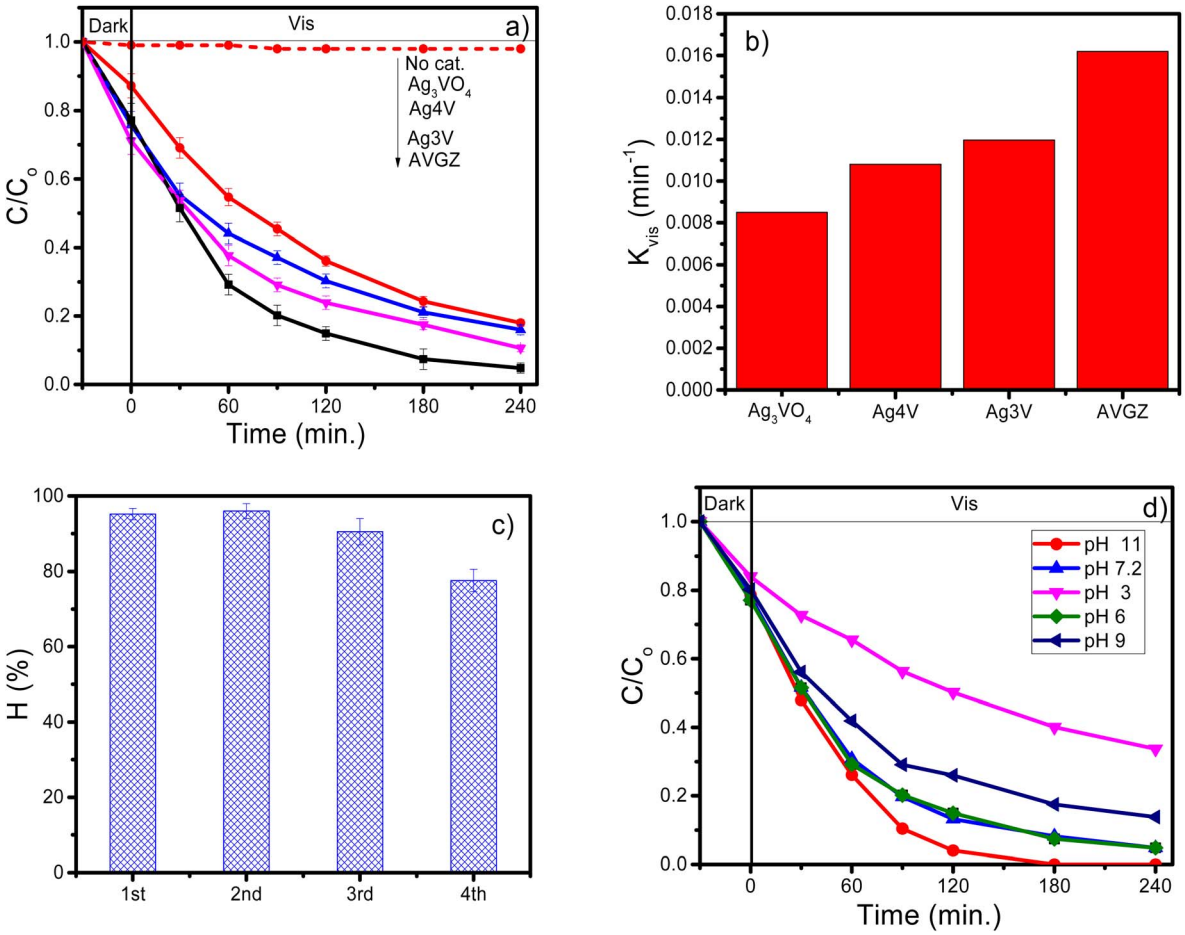

Fig. 6 DDT degradation process on catalysts (a), reaction rate constants (b), catalyst reusability of AVGZ (c), and the effect of pH on the reaction process (d).

facilitated but could reduce the catalyst stability and DDT adsorption ability. At pH 6.0–8.0, the DDT degradation efficiency is considered optimal due to the stability of the catalyst, enhanced adsorbability, and increased production of reactive species, similar to previous reports.[6,7] When pH > 8.0, ·OH radicals are rapidly eliminated, preventing them from having enough time to react with DDT.[38] At pH 11, the OH^- radicals increase, leading to more ·OH radicals through h^+ and OH^- interactions. However, partial decomposition of DDT may occur at excessively high pH, increasing the reaction efficiency but reducing catalyst stability, requiring additional steps to return to neutral conditions before further processing. Therefore, in this study, pH 6 was chosen for subsequent experiments.

3.7. Optimization of DDT degradation process on AVGZ using the RSM method

The second-order optimization model: the Central Composite Design (CCD) method presented in Table S1† was used to design a matrix for 15 experimental runs with 3 repetitions at the centre. In some other studies, the concentration of DDT treated is usually studied <30 mg L^{-1}.[4,7] Additionally, the photocatalytic method is typically used to degrade pollutants at low concentrations, so we fixed the DDT concentration at 10 mg L^{-1}, similar to some previous reports.[3,6] Therefore, the pH variable (B) was investigated in the range of 3.0–9.0, the cat. of the AVGZ catalyst (A) was explored from 0.1–0.5 g L^{-1}, and the reaction time (C) was studied from 0.5 hours to 4.0 hours. The experimental results of 15 runs and predictions by Design-Expert 9 (DX9) are shown in Table S2.† According to the results in Table S2,† the statistical model representing the dependence of the reaction efficiency (H%) on the independent variables (pH, cat., and time) in the photocatalytic DDT degradation process follows the encoded form of the equation as follows:

$$H\,(\%) = 91.04 + 16.57A + 7.95B + 16.20C - 4.88AB + 8.67AC + 7.24BC - 16.61A^2 - 25.27B^2 - 20.42C^2 \quad (1)$$

The values selected and presented in eqn (1) were obtained by using the P-value analysis with $P < 0.05$.[39] The results from Table 2, the ANOVA analysis, show that the second-order model constructed is significant since the model factors such as pH, cat., and time all have P-values meeting the condition $P < 0.05$. The positive and negative values of each coefficient indicate the contribution of the factors in the model related to the reaction efficiency. Accordingly, the larger the positive value or the

Table 2 Analysis of variance (ANOVA) for the quadratic regression model

Source	Sum of squares	df	Mean square	*F*-Value	*p*-Value	
Model	9694.82	9	1077.2	712.7	<0.0001	Significant
A–A	2195.86	1	2195.86	1452.84	<0.0001	
B–B	505.14	1	505.14	334.22	<0.0001	
C–C	2098.55	1	2098.55	1388.45	<0.0001	
AB	95.26	1	95.26	63.02	0.0005	
AC	301.02	1	301.02	199.16	<0.0001	
BC	209.82	1	209.82	138.82	<0.0001	
A^2	1018.42	1	1018.42	673.81	<0.0001	
B^2	2356.95	1	2356.95	1559.42	<0.0001	
C^2	1538.91	1	1538.91	1018.19	<0.0001	
Residual	7.56	5	1.51			
Lack of fit	5.94	3	1.98	2.44	0.3036	Not significant
Pure error	1.62	2	0.8097			
Cor total	9702.38	14				

smaller the negative value, the greater the influence on the process efficiency, and *vice versa*.[39] According to the second-degree equation, all three factors, cat., pH, and time, strongly influence the objective function, with negative coefficients (−16.61, 25.27, and 20.42, respectively). The cat. and pH have a greater impact on the objective function with a higher negative coefficient (−4.88) than the interaction of pH/time and cat./time.

The accuracy and importance of the suggested models were demonstrated by the adjusted R^2 coefficient and the anticipated R^2 coefficient, which showed a discrepancy of less than 0.2 when the model's adequacy was assessed (Table S3†). The adjusted R^2 and predicted R^2 values are 0.997 and 0.989, respectively, confirming that the second-order model is appropriate and provides good accuracy for both theoretical and experimental values. The low CV% value (2.13) indicates the reliability of the experimental data.[40] The experimental *versus* predicted response plot shows minimal deviation between the values. The data presented in Fig. 7a and b also indicate that the model has a good correlation, as the points are concentrated in a straight-line pattern, and the distribution of the experimental points is random, following a normal distribution.[40] These results confirm the completeness and good compatibility of the proposed model with the experimental results, and this model can be used to predict the DDT degradation process on the AVGZ catalyst system.

The influence of factors on DDT removal efficiency is described by three-dimensional (3D) response surface plots and 2D contour plots (Fig. 8a–c, respectively). The red area represents the highest DDT removal efficiency, while the blue area indicates lower results. Each plot has an optimal region, suggesting that DDT treatment efficiency depends on the initial catalyst concentration, solution pH, and reaction time. Generally, as the catalyst concentration and reaction time increase, DDT degradation efficiency increases (Fig. 8a). This increasing trend is attributed to the enhanced active sites and adsorption capability of the catalyst.[41] The results also confirm that as reaction time increases, efficiency improves due to the higher production of reactive species.[40]

Fig. 8b and c show the correlation between pH and cat., as well as pH and reaction time, concerning DDT degradation efficiency. The effect of solution pH shows that DDT

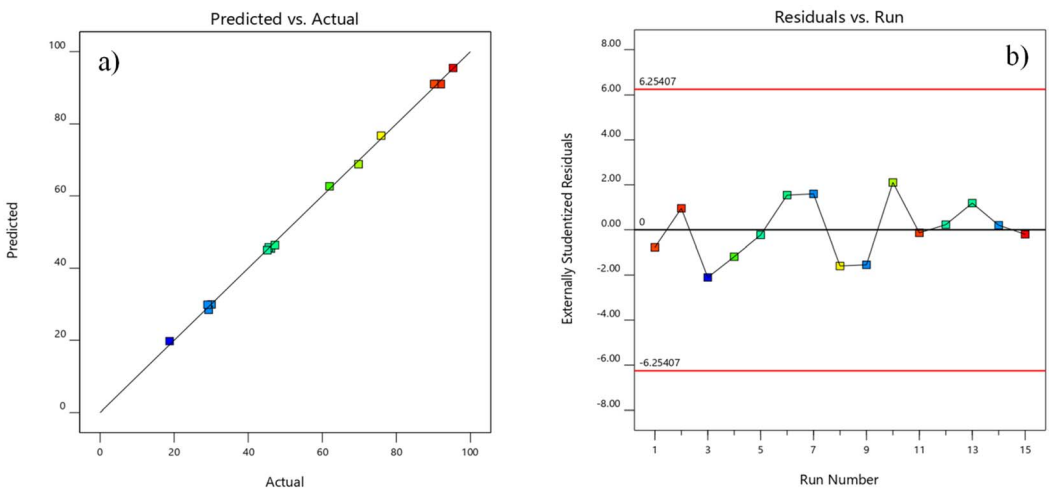

Fig. 7 Experimental-predicted value plot (a) and random distribution of 15 experiments (b).

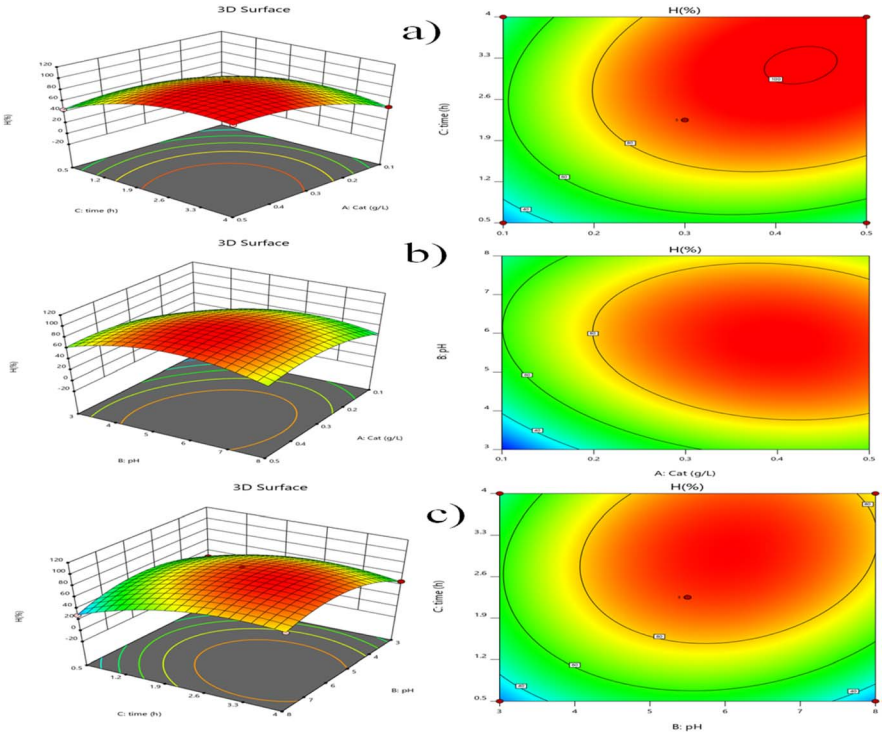

Fig. 8 Surface (3D) and contour (2D) plots for the photocatalytic degradation of DDT on AVGZ catalyst (a–c).

degradation efficiency increases when pH rises from 3.0 to 7.0 and decreases at higher values. Typically, increasing pH leads to a rise in ·OH radicals, facilitating the formation of hydroxyl radicals, which enhances the reaction efficiency.[42] However, for DDT, this trend is reversed. This can be explained by the zeta potential of AVGZ (Fig. S4†) and the existence of DDT in different pH forms. DDT is a nonpolar organic chlorine compound with low dissociation in water, and thus does not exhibit distinct ionization states like strong acids or bases. The surface of AVGZ is believed to be electrically neutral in the pH range of 5.0–7.0, which enhances DDT adsorption onto the catalyst surface, promoting interaction between the catalyst's active sites and DDT. At lower or higher pH levels, reactive species may increase, causing competitive adsorption between the electrostatic surface of the catalyst and DDT, reducing the process efficiency.[41]

From the data in Fig. 8a–c and applying the DX9 optimization software, the optimal conditions, including cat., reaction time, and solution pH, are listed in Table S4,† with the highest desirability value of 1.0. Under these conditions, the degradation rate achieved is 95.46% for DDT, with no significant difference at the 95% confidence level between predicted and experimental degradation under optimal conditions. This demonstrates the success of the model in optimizing the DDT degradation process on AVGZ.[43]

3.8. Photocatalytic mechanism of DDT degradation on the AVGZ catalyst

To further investigate the role of reactive radicals such as h^+, ·OH, and $\cdot O_2^-$ in the DDT degradation process, different radical scavengers such as AO, pBQ, and TBA were added as trapping agents in the reaction system (Fig. 9a).[19] For the AVGZ and Ag3V catalytic systems, before adding radical scavengers, the DDT degradation efficiency was 95.2% and 89.4%, respectively. When AO (h^+) and PBQ ($\cdot O_2^-$) were introduced, the DDT degradation efficiency decreased, especially in the presence of PBQ. In the AVGZ system, the degradation efficiency dropped to 65.1% and 48.6%, while for Ag3V, it decreased to 63.5% and 50.3%, respectively. In contrast, for Ag_3VO_4, the degradation efficiency dropped significantly in the presence of AO (30.6%) and slightly decreased when using pBQ (70.7%).[24] The addition of TBA resulted in a mild decrease in the degradation efficiency for Ag_3VO_4 (77.3%) and a more significant reduction for Ag3V (73.1%) and AVGZ (60.1%), respectively. These results indicate that for Ag_3VO_4, the h^+ radicals play a dominant role in the photocatalytic reaction. For Ag3V and AVGZ, all radicals participate in the response, with the trend being $\cdot O_2^-$ > (h^+ and ·OH). Among these, AVGZ exhibits a more substantial presence of $\cdot O_2^-$ and ·OH than Ag3V. This finding was further confirmed by EPR trapping techniques in Fig. 9b and c. The free radicals were trapped using DMPO and dispersed in methanol and aqueous solution in the presence of the catalyst under light irradiation. The results showed that the intensity of DMPO-OH and DMPO-O_2^- signals for Ag_3VO_4 were lower than those for Ag3V and AVGZ, respectively, confirming that $\cdot O_2^-$ and ·OH are the key species in the photocatalytic degradation of DDT.[19,24]

As previously noted, the valence band potential (E_{vb}) and conduction band potential (E_{cb}) are calculated using the following formulae:[44,45]

$$E_{vb} = E_{cb} + E_{bg} \quad (2)$$

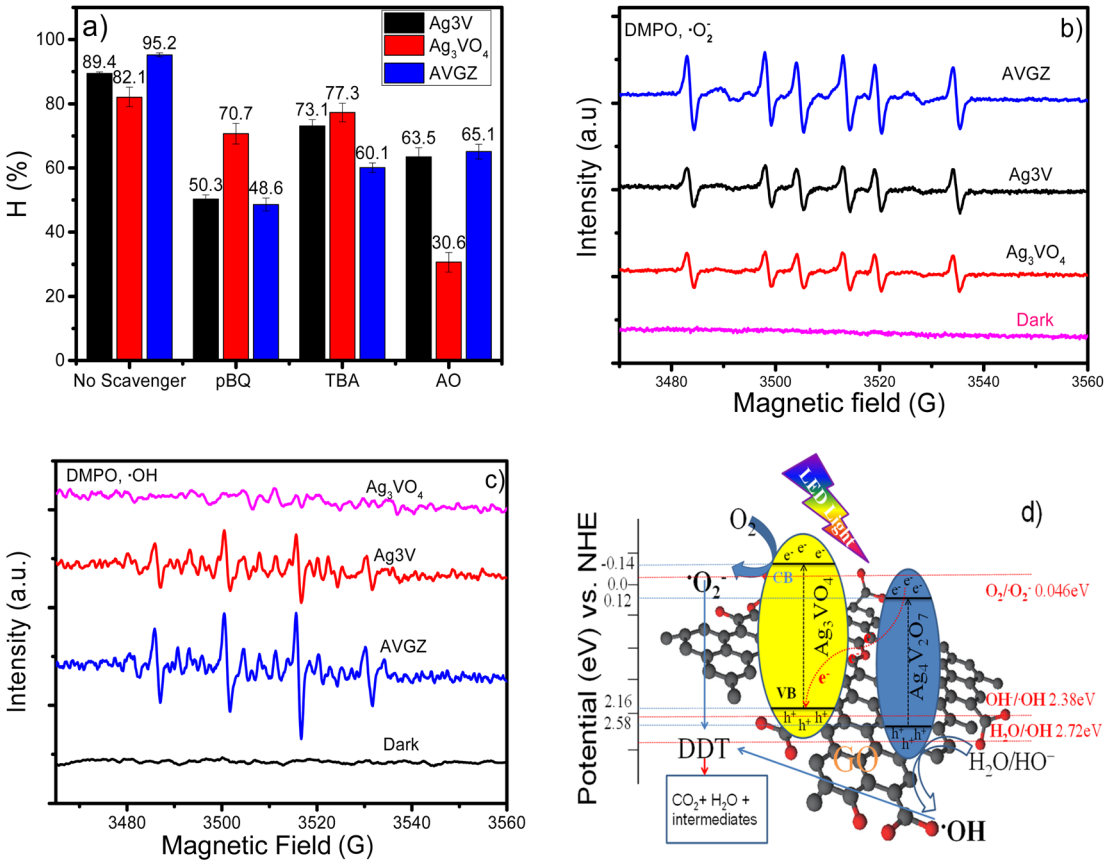

Fig. 9 The effect of oxidation inhibitors (a), spin trapping of $\cdot O_2^-$ and ·OH with DMPO (b and c), and the proposed mechanism for the degradation of DDT on AVGZ (d).

$$E_{NHE} = E_{Ag/AgCl} + 0.2\ eV \quad (3)$$

The E_{bg} of Ag_3VO_4 is 2.32 eV, and the $E_{Ag/AgCl}$ of Ag_3VO_4 is −0.24 eV (Fig. S5a†). Therefore, the standard hydrogen electrode (E_{NHE}) potential of Ag_3VO_4 is −0.04 eV. For n-type semiconductors, the E_{cb} potential is more damaging than the E_{NHE} by 0.1 eV, so the E_{cb} of Ag_3VO_4 is −0.14 eV,[46] and the E_{vb} is 2.18 eV, respectively. Thus, Ag_3VO_4 can reduce O_2 in water to form $\cdot O_2^-$ ($O_2/\cdot O_2^-$ is −0.046 eV/NHE).[38,47]

For $Ag_4V_2O_7$, the $E_{Ag/AgCl}$ value is 0.02 eV, corresponding to 0.22 eV/NHE (Fig. S5b†). Therefore, the E_{cb} of the n-type $Ag_4V_2O_7$ semiconductor is 0.12 eV/NHE, and the E_{vb} is 2.60 eV/NHE.[27] The analysis results show that the E_{cb} and E_{vb} of Ag_3VO_4 are both more negative than those of $Ag_4V_2O_7$, respectively. If the electron transfer pathway of the three-component system follows the traditional heterojunction mechanism, the electrons (e^-) in the conduction band (CB) will transfer from Ag_3VO_4 to $Ag_4V_2O_7$ *via* GO during the photocatalytic reaction, and the holes h^+ in the valence band (VB) will transfer back from $Ag_4V_2O_7$ to Ag_3VO_4. However, the electrons in the CB of $Ag_4V_2O_7$ cannot reduce O_2 to $\cdot O_2^-$ because the E_{cb} of 0.12 eV (the potentials of $O_2/\cdot O_2^-$ is −0.046 to −0.33 eV/NHE).[48–50] If we apply this theory, the h^+ radicals will become the main reactive species, which contradicts the radical trapping and EPR experiments. Therefore, the Z-scheme mechanism for the AVGZ photocatalyst is proposed as follows: the electrons in the CB of $Ag_4V_2O_7$ are rapidly transferred to the VB of Ag_3VO_4 *via* the electron transfer channel of GO. Here, the electrons recombine with h^+ and e^- in Ag_3VO_4 are enhanced, enabling the formation of $\cdot O_2^-$ radicals. On the other hand, h^+ in the VB of $Ag_4V_2O_7$ cannot directly oxidize H_2O but can react with OH^- to generate ·OH radicals (·OH/H_2O of 2.72 eV, ·OH/OH^- of 2.38 eV).[50,51] The process mechanism is shown in Fig. 9d and eqn (4)–(8).

$$Ag_3VO_4 + h\nu \rightarrow Ag_3VO_4\ (e^-/h^+) \quad (4)$$

$$Ag_4V_2O_7\ (e^-/h^+) + Ag_3VO_4 + h\nu \rightarrow Ag_3VO_4\ (e^-/h^+) \rightarrow (GO) \rightarrow Ag_4V_2O_7\ (h^+) + Ag_3VO_4\ (e^-) \quad (5)$$

$$Ag_3VO_4\ (e^-) + O_2 \rightarrow Ag_3VO_4 + \cdot O_2^- \quad (6)$$

$$Ag_4V_2O_7\ (h^+) + OH^-/H_2O \rightarrow \cdot OH \quad (7)$$

$$\cdot O_2^- + h^+ + \cdot OH + DDT \rightarrow CO_2 + H_2O + intermediates \quad (8)$$

As is well known, the reaction rate constants for the ·OH with POPs in liquid environments range from 10^9 to 10^{10} M^{-1} s^{-1}.[52] The reaction rate constant for the $\cdot O_2^-$ is approximately 2.5–6.8 × 10^7 M^{-1} s^{-1}.[53] Therefore, the ·OH first attacks and breaks functional groups. Afterwards, ·OH radicals attack aromatic rings to form hydroxycyclohexadienyl radicals. Due to

the electrophilic nature of ·OH, the attack on aromatic rings is faster when these rings contain activated groups such as –OH or $–NR_2$.[52] Organic radicals (·R) are formed, which then participate in a series of chain reactions, both propagating and terminating, leading to organic compounds, peroxyl radicals in oxygen-free conditions, and inorganic compounds or mineral salts in the reaction environment. Thus, the degradation products of DDT primarily undergo chlorination first, followed by ring cleavage into shorter carbon chain compounds ($C_{14}H_{10}Cl_4$, *m*,*p*′-DDD, $C_9H_6Cl_6$, buta-1,3-diene-1,2,3,4,5,5-hexachlorocyclopenta-1,3-diene (1/1), $C_9H_{11}NO_2$, ethyl 3-pyridylacetate, $C_8H_7NO_3$, 2-(2-nitrovinyl)phenol, respectively) (Fig. S6†).[2] This can be explained by the fact that the C–Cl bond, with a bond energy of 327 kJ mol^{-1}, is weaker than the C–H, C–C, and C=C bonds, making it more easily broken. After the C–Cl bond is broken, the C–C (346 kJ mol^{-1}) and C–H (411 kJ mol^{-1}) bonds are then broken to form shorter hydrocarbon compounds. Finally, the C=C bonds in the aromatic rings, which have higher bond energies (602 kJ mol^{-1}), are more challenging to break and remain intact.[54]

4. Conclusion

The AVGZ and Ag3V nanocatalysts, with a 5.0% GO content, were synthesized using a hydrothermal method combined with a microwave-assisted technique. By adjusting the pH, the phase composition of Ag_3VO_4 and $Ag_4V_2O_7$ in the nanocomposite structure could be well controlled. The XRD, BET, TEM, and XPS analysis confirmed that the presence of GO increases the surface area, prevents the agglomeration of Ag_3VO_4 and $Ag_4V_2O_7$ NPs, and forms M–O–C bonds, which serve as electron transfer channels from NPs to GO. The UV-Vis, EIS, and PL analyst results demonstrated the extension of the visible light absorption region, a decrease in the E_{bg} and inhibition of e^-/h^+ recombination in the AVGZ heterostructure.

The photocatalytic activity for DDT degradation of AVGZ and Ag3V was higher than that of pure Ag_3VO_4 and Ag4V. Under the same reaction conditions, the DDT degradation efficiency reached 95.2% for AVGZ and 89.4% for Ag3V, respectively. The experimental results were consistent with ANOVA analysis, confirming that the quadratic DDT degradation model on AVGZ was significant with a *P*-value < 0.05. The synergistic effect between GO and $Ag_3VO_4/Ag_4V_2O_7$ inhibits the photo corrosion of individual crystal phases and can maintain the reaction efficiency after four cycles for AVGZ. Based on structural band analysis and electron transfer pathways, we propose that charge transfer in the AVGZ catalyst system follows a Z-scheme.

Data availability

The corresponding author can provide the datasets created and examined in this study upon reasonable request.

Author contributions

Giang H. Le: project administration, methodology, writing – original draft, supervision. Duong A. Thanh: software, formal analysis, data curation. Trang T. T. Pham: methodology, funding acquisition, conceptualization. Quang Vinh Tran: investigation, formal analysis. Nhiem Ngoc Dao: writing – review & editing, software. Kien Trung Nguyen: resources, investigation, formal analysis. Trang T. T. Quan: writing – review & editing, validation, supervision.

Conflicts of interest

The authors state that none of their personal ties or known conflicting financial interests might have appeared to have influenced the work described in this study.

References

1 R. Guardans, *Environ. Sci.:Adv.*, 2024, **3**, 1111–1123.
2 G. H. Le, T. T. Nguyen, M. B. Nguyen, T. T. T. Quan, T. D. Nguyen, A. Sapi, I. Szenti, S. Mutyala, A. Kukovecz, Z. Konya and T. A. Vu, *Top. Catal.*, 2020, **63**, 1314–1324.
3 T. T. Nguyen, G. H. Le, C. H. Le, M. B. Nguyen, T. T. T. Quan, T. T. T. Pham and T. A. Vu, *Mater. Res. Express*, 2018, **5**, 115005.
4 M. Dang, D. Chen, P. Lu and G. Xu, *Chemosphere*, 2022, **307**, 135893.
5 H. D. Rizqi, A. S. Purnomo and A. Ulfi, *Heliyon*, 2023, **9**, e18216.
6 N. D. Van, H. T. Khuyen, N. M. Ha, N. V. Dung and H. T. H. Ngoc, *Chem. Eng. J.*, 2023, **466**, 143232.
7 N. Alhokbany, T. Ahamad, J. Ahmed and S. M. Alshehri, *Mater. Lett.*, 2022, **319**, 132271.
8 C. Lin and K.-S. Lin, *Chemosphere*, 2007, **66**, 1872–1877.
9 M. H. El-Saeid, A. BaQais and M. Alshabanat, *Molecules*, 2022, **27**(3), 634.
10 P. Kajitvichyanukul, V.-H. Nguyen, T. Boonupara, L.-A. Phan Thi, A. Watcharenwong, S. Sumitsawan and P. Udomkun, *Environ. Res.*, 2022, **212**, 113336.
11 S. R. Tariq, Z. Niaz, G. A. Chotana, D. Ahmad and N. Rafique, *RSC Adv.*, 2023, **13**, 19326–19334.
12 P. Rosaiah, D. Yue, L. Harikrishnan, A. A. Ghfar, M. Dhananjaya and S. W. Joo, *J. Alloys Compd.*, 2024, **989**, 174326.
13 H. Zhang, Y. Gao, S. Meng, Z. Wang, P. Wang, Z. Wang, C. Qiu, S. Chen, B. Weng and Y.-M. Zheng, *Adv. Sci.*, 2024, **11**, 2400099.
14 A. Shabbir, S. Sardar and A. Mumtaz, *J. Alloys Compd.*, 2024, **1003**, 175683.
15 A. Chauhan, N. Sonu, P. Raizada, P. Singh, T. Ahamad, V.-H. Nguyen, Q. Van Le, A. Aslam Parwaz Khan, N. Kumar, A. Sudhaik and C. Mustansar Hussain, *J. Ind. Eng. Chem.*, 2024, **130**, 25–53.
16 C.-C. Chen, J. Shaya, H.-J. Fan, Y.-K. Chang, H.-T. Chi and C.-S. Lu, *Sep. Purif. Technol.*, 2018, **206**, 226–238.
17 M. H. T. Tung, T. T. T. Phuong, D. M. N. Tram, D. M. The, N. V. N. Mai, T. T. T. Hien, L. T. C. Nhung, N. T. T. Binh, C. Van Hoang, D. N. Nhiem, T.-D. Pham and N. T. D. Cam, *Diamond Relat. Mater.*, 2022, **121**, 108788.

18 Z. I. Zaki, M. S. Amin, R. M. Mohamed and I. A. Mkhalid, *J. Inorg. Organomet. Polym. Mater.*, 2021, **31**, 2999–3010.
19 J. Wang, P. Wang, Y. Cao, J. Chen, W. Li, Y. Shao, Y. Zheng and D. Li, *Appl. Catal., B*, 2013, **136–137**, 94–102.
20 M. Gao, L. Sun, C. Ma, X. Li, H. Jiang, D. Shen, H. Wang and P. Huo, *Inorg. Chem.*, 2021, **60**, 1755–1766.
21 D. P. Das, R. K. Barik, J. Das, P. Mohapatra and K. M. Parida, *RSC Adv.*, 2012, **2**, 7377–7379.
22 H. Uk Lee, S. C. Lee, J. Won, B.-C. Son, S. Choi, Y. Kim, S. Y. Park, H.-S. Kim, Y.-C. Lee and J. Lee, *Sci. Rep.*, 2015, **5**, 8691.
23 H. T. Vu, L. T. Tran, G. H. Le, Q. K. Nguyen, T. M. Vu and T. A. Vu, *Vietnam J. Chem.*, 2019, **57**, 681–685.
24 Y. Wang, M. Wu, W. Lei, Y. Shen, F. Li and C. Peng, *J. Alloys Compd.*, 2022, **895**, 162410.
25 A. Vali, S. Y. Kim, F. Danladi, A. Rawat, C. Zhang, P. S. Toth, C. Janáky, N. Myung, E. I. Meletis and K. Rajeshwar, *J. Electrochem. Soc.*, 2023, **170**, 052504.
26 R. Ran, J. G. McEvoy and Z. Zhang, *Mater. Res. Bull.*, 2016, **74**, 140–150.
27 Y. Xing, X. Lu, Y. Li, B. Yang, Y. Huang, M. Zhang, J. Cheng, X. Min and W. Pan, *J. Adv. Ceram.*, 2022, **11**, 1789–1800.
28 C. Ren, J. Fan, S. Liu, W. Li, F. Wang, H. Li, X. Liu and Z. Chang, *RSC Adv.*, 2016, **6**, 95156–95164.
29 C.-M. Huang, G.-T. Pan, Y.-C. M. Li, M.-H. Li and T. C. K. Yang, *Appl. Catal., A*, 2009, **358**, 164–172.
30 B. H. Fard, R. R. Khojasteh and P. Gharbani, *J. Inorg. Organomet. Polym. Mater.*, 2018, **28**, 1149–1157.
31 B. Zhai, Y. Chen and Y. Liang, *J. Nanopart. Res.*, 2019, **21**, 265.
32 R. Ran, X. Meng and Z. Zhang, *Appl. Catal., B*, 2016, **196**, 1–15.
33 H. Zhu, Q. Ren, Y. Ding, C. Zhu, Y. Zong, X. Hu and Z. Jin, *Inorg. Chem. Commun.*, 2021, **131**, 108759.
34 H. Huang, J. Zhao, H. Guo, B. Weng, H. Zhang, R. A. Saha, M. Zhang, F. Lai, Y. Zhou, R.-Z. Juan, P.-C. Chen, S. Wang, J. A. Steele, F. Zhong, T. Liu, J. Hofkens, Y.-M. Zheng, J. Long and M. B. J. Roeffaers, *Adv. Mater.*, 2024, **36**, 2313209.
35 W. Cheng, L. Wang, H. Lao, Y. Wei, J. Xu and B. Weng, *ACS Sustain. Chem. Eng.*, 2024, **12**, 17026–17034.
36 H. Huang, J. Zhao, B. Weng, F. Lai, M. Zhang, J. Hofkens, M. B. J. Roeffaers, J. A. Steele and J. Long, *Angew. Chem., Int. Ed.*, 2022, **61**, e202204563.
37 X. Liu, G. Dawson, K. Papadikis and P.-S. Yap, *J. Ind. Eng. Chem.*, 2025, **145**, 561–576.
38 K. Meskelu, A. M. Taddesse, E. Teju and Z. Bezu, *Results Chem.*, 2024, **11**, 101786.
39 M. El Ouardi, V. Madigou, V. Chevallier, A. Merlen, A. BaQais, M. Saadi, H. Ait Ahsaine and M. Arab, *J. Environ. Chem. Eng.*, 2024, **12**, 113505.
40 K. M. Batoo, K. H. Jassim, T. A. Qassem, S. Hussain, W. Talib Hasson, S. S. Jalal, M. F. Ramadan, S. M. Hameed, A. H. Alawadi and A. Alsaalamy, *J. Saudi Chem. Soc.*, 2024, **28**, 101871.
41 H. Zolfaghari, F. Yousefi, M. Ghaedi and S. Mosleh, *RSC Adv.*, 2022, **12**, 29503–29515.
42 H. Sheikhpoor, A. Saljooqi, T. Shamspur and A. Mostafavi, *Environ. Technol. Innovation*, 2021, **23**, 101649.
43 H. Abbasi_Asl, M. M. Sabzehmeidani, M. Ghaedi and Z. Moradi, *J. Environ. Manage.*, 2023, **345**, 118656.
44 S. Wang, D. Li, C. Sun, S. Yang, Y. Guan and H. He, *Appl. Catal., B*, 2014, **144**, 885–892.
45 Y. Xie, Y. Dai, X. Yuan, L. Jiang, L. Zhou, Z. Wu, J. Zhang, H. Wang and T. Xiong, *J. Colloid Interface Sci.*, 2018, **530**, 493–504.
46 M. Zohari-Moafi, A. Habibi-Yangjeh, M. Habibi and Y. Akinay, *Mol. Catal.*, 2024, **556**, 113920.
47 M. Habibi, A. Habibi-Yangjeh and A. Khataee, *Surf. Interfaces*, 2023, **39**, 102937.
48 P. Zhu, J. Lin, L. Xie, M. Duan, D. Chen, D. Luo and Y. Wu, *Langmuir*, 2021, **37**, 13309–13321.
49 J. Xiong, H.-Y. Zeng, C.-R. Chen, S. Li, S. Xu and D.-S. An, *Appl. Clay Sci.*, 2021, **208**, 106118.
50 Y. Hu, J. Fan, C. Pu, H. Li, E. Liu and X. Hu, *J. Photochem. Photobiol., A*, 2017, **337**, 172–183.
51 G. Fan, X. Li, J. Lin, X. Wu, L. Zhang, J. Wu and Y. Wang, *Sep. Purif. Technol.*, 2022, **299**, 121803.
52 L. Wojnárovits and E. Takács, *Radiat. Phys. Chem.*, 2014, **96**, 120–134.
53 B. Maillard, K. U. Ingold and J. C. Scaiano, *J. Am. Chem. Soc.*, 1983, **105**, 5095–5099.
54 U. H. Hossain, T. Seidl and W. Ensinger, *Polym. Chem.*, 2014, **5**, 1001–1012.